PAPER

Contribution of frictional contact during steady and oscillatory shear in the discontinuous shear thickening fluid

IOP Publishing Smart Materials and Structures
Smart Mater. Struct. **28** (2019) 045009 (14pp) https://doi.org/10.1088/1361-665X/ab04b5

Contribution of frictional contact during steady and oscillatory shear in the discontinuous shear thickening fluid

Kaihui Chen, Yu Wang[1,2], Shouhu Xuan, Saisai Cao and Xinglong Gong[1,2]

CAS Key Laboratory of Mechanical Behavior and Design of Materials, Department of Modern Mechanics, CAS Center for Excellence in Complex System Mechanics, University of Science and Technology of China, Hefei, Anhui 230027, People's Republic of China

E-mail: wyu@ustc.edu.cn and gongxl@ustc.edu.cn

Received 28 November 2018, revised 15 January 2019
Accepted for publication 6 February 2019
Published 14 March 2019

Abstract

In the present work, an elastic-core-modified mesoscale dissipative particle dynamics model is proposed, so as to investigate the microstructural evolution dependency on the viscosity in shear thickening fluids. The characteristic of the microstructural evolution in the colloidal suspensions under steady shear deformation is studied. The dominant interaction in the system changes from the hydrodynamics to the strong frictional contacts during the discontinuous shear thickening (DST) stage. An oscillatory shear action is creatively taken to study the rheological properties of the suspension, as well as to investigate the microstructural evolution with dynamic response of the system. The exact formulation of the relative viscosity as a function of the effective volume fraction (EVF), which is obtained from the packaging of the frictional contact network, is proposed. It is confirmed that the formation of frictional contact network of dispersed colloidal particles is determined by the competition between construction and decomposition of the particle contacts. The influences of different factors, like particle size, volume fraction, and surface roughness, on the DST behavior are also explored to prove our mechanism. The relationship of shear rate, frictional contact network, EVF, and apparent viscosity is revealed clearly.

Keywords: discontinuous shear thickening, microstructure, effective volume fraction, frictional contact network

(Some figures may appear in colour only in the online journal)

1. Introduction

Shear thickening fluid (STF) is a collective name for smart materials with a remarkable non-Newtonian rheological behavior, of which the apparent viscosity starts to increase when the shear rate exceeds a specific value [1–3]. Great deals of research [4–6] are conducted to explain the shear thickening (ST) effect in different suspension systems under shear, and a picture of ST phenomenon has emerged [7–15]. Hoffman [16] thought that the transition of flow microstructure from an ordered structure to a disordered one is responsible for the ST behavior. While, with confocal imaging techniques, Wagner and other researchers [17–25] concluded that in suspensions the formation of 'hydro-cluster', long-lived particle clusters, is the primary cause for the continuous shear thickening (CST) phenomenon. And the competition between the shear-induced cluster formation and the Brownian motion in the suspensions can be used to determine a critical shear rate for the onset of the ST phenomenon. Jamali *et al* [10] studied the hydrodynamic contributions of colloidal particles with different stiffness through numerical simulation, and they also took the first normal stress difference to characterize the properties of the dispersed particles under shear. The role of hydrodynamics

[1] Author to whom any correspondence should be addressed.
[2] These authors made equal contribution.

contributions during the ST phenomenon has been explored very thoroughly [26–31].

When the Brownian motion is absent in some suspensions with large particles, the sharp discontinuous shear thickening (DST) transition is observed. The increase of apparent viscosity is both sudden and large with the shear rate beyond a certain value. As is reported in many types of research [32, 33], dense suspensions show highly DST behaviors with little changes in the component of the system, which show CST originally. Over the past few years, the DST behavior has been the focus of sustained research efforts and particle contact was considered by more and more researchers [34–40]. In addition, many people [41, 42] also believed that jamming and shear-jammed status take a key role in this non-Newtonian behavior. Some researcher [36, 38] associated the frictional contact and the jamming to explain this process, Peter and partners [34] suggested that the DST state is an independent phenomenon from shear-jammed transitions and jamming states, and they confirmed that the frictional contacts between particles do impact on the DST behavior. Townsend [39] studied steady-state rheological properties of non-Brownian suspensions and the effects of different frictional contact modulus, and they estimated that soft or compressible contacting is a key reason for DST effect in the experiment. Mari *et al* [36] focused on the formation of contact networks in STFs, and they associated the DST behavior with S-shaped flow curves [40]. The existing simulations are more qualitatively studying the mechanism of ST, failing to completely reproduce the experimental process and the data of the results.

Actually, from above results, the DST behaviors are closely related with the dynamic and interactions of colloidal particles in the viscous fluids. Much efforts has been conducted on these two aspects [43–45]. Faltas [43] and Saad [44] explored the translational and rotational motions of two spherical particles with slip at surfaces. They adopted various cases of the slip coefficients, the translational velocity, the angular velocity, the separation parameter and the size ratio of the two spherical particles to obtain accurate solutions. They proposed the monotonical function of the impact of the slip and the normalized hydrodynamics drag and couple. El-Sapa and coworkers [45] also confirmed that the interaction effect between particles decreases with the increase of both the slip parameters and the permeability parameter via their effective-medium approach.

Although, plenty of experimental and numerical works have concerned on the reason for the DST behavior [14, 40–53]. The internal mechanism and conditions of emergence of DST phenomenon remain ill-characterized. The effect of the interactions between colloidal particles on the DST behaviors is still in lack of study. To make the mechanism credible and valid, it is necessary to deeply investigate the microstructure of the STFs. In this paper, the non-Newtonian rheological behavior of STF under steady and dynamic shear is conducted by a modified dissipative particle dynamics (DPD) model. In the next section, the modified DPD model concerned about the contact interaction between colloidal particles is briefly reviewed, and then the details of the computation model are introduced. In section 3, the non-Newtonian rheological behavior of dense suspensions under steady shear and the microstructural change of colloidal particles in ST process are studied, followed by the viscoelasticity properties and microstructural evolution of STF under oscillatory shear. The evolutions of the contact network of suspensions under oscillation are also analyzed. The connection between the relative viscosity and the effective volume fraction (EVF) within ST behavior, bridging by the frictional contact force and the contact network, is deeply discussed throughout this section as well. In section 4, the influence of volume fraction, particle size, and surface roughness on the DST are also displayed to prove the relationship concluded in section 3. Finally, the conclusion of the simulation results is drawn in the last section.

2. Simulation method

2.1. Modified DPD model

The DPD technique is an alternative method for mesoscopic complex fluid simulation, which was first developed for simulating hydrodynamic behavior by Hoogerbrugge and Koelman [15]. In traditional DPD models, the dissipative particles need not correspond to real particles, in some cases, they can be interpreted as representations of 'groups of atoms'. There are three types of forces to describe the interaction between different dissipative particles in the model: a conservative force $\boldsymbol{F}_{ij}^{C}$ deriving from a potential, a dissipative force $\boldsymbol{F}_{ij}^{D}$ that tries to reduce radial velocity differences between the particles, and a further stochastic force $\boldsymbol{F}_{ij}^{S}$ directed along the line joining the center of the particles. The last two forces are momentum conserving, which represent the viscous forces and thermal noises between the dissipative particles. Most rheology behaviors in suspension have been successfully mimicked by the traditional DPD model [15, 54–57].

However, in the dense suspensions, the frictional contact between dispersed solute particles is the main reason for the DST behaviors, which has not been not correctly characterized in the traditional DPD model. Therefore, a modified DPD model is proposed here to describe the diverse interactions in the colloidal systems. And frictional contact interactions between different colloidal particles are included.

In the modified DPD model, the motion equation for the particles is expressed as:

$$m_i \frac{d\boldsymbol{V}_i}{dt} = \sum_{j \neq i} (\boldsymbol{F}_{ij}^{C} + \boldsymbol{F}_{ij}^{S} + \boldsymbol{F}_{ij}^{D} + \boldsymbol{F}_{ij}^{Contact}). \tag{1}$$

The conservative force is a linearly-decaying repulsive function for the interaction between particles, which is always denoted as:

$$\mathbf{F}_{ij}^{C} = a_{ij}\left(1 - \frac{r_{ij}}{r_c}\right)\boldsymbol{e}_{ij}, \tag{2}$$

in which r_c is the cutoff distance, r_{ij} is the distance between particle i and j, and $\boldsymbol{e_{ij}}$ is the unit vector as $\boldsymbol{e_{ij}} = \boldsymbol{r}_{ij}/|\boldsymbol{r}_{ij}|$, $\boldsymbol{r}_{ij} = \boldsymbol{r}_i - \boldsymbol{r}_j$ [54]. The a_{ij} is an empirical constant, which is given as $a_{ij} \approx K_{\mathrm{B}}T(k^{-1} - 1)/(0.2\rho)$, where K_{B} is the

Boltzmann constant, T is the temperature, k^{-1} is the dimensionless compressibility of the suspension, and ρ is the total number density of the DPD particles [55].

The stochastic force is related the thermal fluctuations to simulate the Brownian motion in systems. The formula of stochastic force between particle i and j is given by:

$$\boldsymbol{F}_{ij}^{S} = b_{ij}\left(1 - \frac{r_{ij}}{r_c}\right)\Theta_{ij}(\Delta t)^{-\frac{1}{2}}\boldsymbol{e}_{ij}, \tag{3}$$

where b_{ij} is the strength of thermal fluctuations of the system, Δt is the time step used in the simulation, and Θ_{ij} is a Gaussian stochastic number with zero mean value and unit variance.

The dissipative force usually acts as friction and collision of inter-particles to dissipate the energy in systems. This force is against with the relative velocity between particle i and j, $\boldsymbol{v}_{ij} = \boldsymbol{v}_i - \boldsymbol{v}_j$. The formulation of the dissipative force is given by:

$$\boldsymbol{F}_{ij}^{D} = -\gamma_{ij}\left(1 - \frac{r_{ij}}{r_c}\right)^2(\boldsymbol{v}_{ij}\cdot\boldsymbol{e}_{ij})\boldsymbol{e}_{ij}, \tag{4}$$

in which γ_{ij} is the dissipative parameter. To ensure the canonical ensemble, there is a built-in thermostat in DPD potential. Therefore, the random force and the dissipative force should meet the fluctuation–dissipation theorem: ${b_{ij}}^2/2\gamma_{ij} = K_{\mathrm{B}}T$ [55].

A Hooke-core model is adopted here to describe the contact interaction between the colloidal particle [57]. The contact force ${\boldsymbol{F}_{ij}}^{Contact}$ between different colloidal particles is divided into two parts, the normal contact force, ${\boldsymbol{F}_{N,ij}}^{Contact}$, and the tangential contact force, ${\boldsymbol{F}_{T,ij}}^{Contact}$:

$${\boldsymbol{F}_{N,ij}}^{Contact} = k_n\delta n_{ij}\boldsymbol{e}_{ij}, \tag{5}$$

$${\boldsymbol{F}_{T,ij}}^{Contact} = k_t\Delta\boldsymbol{s}_{ij}, \tag{6}$$

where k_n and k_t are the normal and tangential elasticity constants, respectively, and δn_{ij} represents the reduction of the core distance between particle i and j due to the normal elastic deformation, and $\Delta\boldsymbol{s}_{ij}$ denotes the tangential displacement vector between particle i and j.

The frictional contact behavior between different colloidal particles is represented as follows: the tangential displacement of the colloidal particle is calculated based on a Coulomb's style friction critical condition, which is given by:

$$|{\boldsymbol{F}_{T,ij}}^{Contact}| \leqslant \mu|{\boldsymbol{F}_{N,ij}}^{Contact}|, \tag{7}$$

of which μ is the Coulomb's friction coefficient. If the Coulomb's law of equation (7) is fulfilled, the particles do not slip with each other, and the tangential displacement is updated through the relative tangential velocity of particles: $\Delta\boldsymbol{s}_{ij} = {\boldsymbol{v}_{ij}}^{\mathrm{T}}dt$, where ${\boldsymbol{v}_{ij}}^{\mathrm{T}} = \boldsymbol{e}_{ij}\times(\boldsymbol{v}_i - \boldsymbol{v}_j)\times\boldsymbol{e}_{ij}$. If not, the particles are sliding and the tangential displacement is dependent on the normal contact force: $|\Delta\boldsymbol{s}_{ij}| = \mu|{\boldsymbol{F}_{N,ij}}^{Contact}|/k_t$. The position, velocity, and acceleration of ith DPD particle (including both solvent and colloidal particles) at time $t + \Delta t_{MD}$ are obtained from the same quantities at time t in the following way:

$$\boldsymbol{r}_i(t + \Delta t_{MD}) = \boldsymbol{r}_i(t) + \boldsymbol{v}_i(t)\Delta t_{MD} + \frac{1}{2}\boldsymbol{a}_i(t)(\Delta t_{MD})^2, \tag{8}$$

$$\boldsymbol{v}_i\left(t + \frac{\Delta t_{MD}}{2}\right) = \boldsymbol{v}_i(t) + \frac{1}{2}\boldsymbol{a}_i(t)\Delta t_{MD}, \tag{9}$$

$$\boldsymbol{a}_i(t + \Delta t_{MD}) = -\frac{1}{m}\boldsymbol{F}_i(\boldsymbol{r}_i(t + \Delta t_{MD})), \tag{10}$$

$$\boldsymbol{v}_i(t + \Delta t_{MD}) = \boldsymbol{v}_i\left(t + \frac{\Delta t_{MD}}{2}\right) + \frac{1}{2}\boldsymbol{a}_i(t + \Delta t_{MD})\Delta t_{MD}. \tag{11}$$

The position and velocity between the colloidal particle is firstly expressed as follows:

$$\boldsymbol{r}_{ij}(t + \Delta t_{MD}) = \boldsymbol{r}_i(t + \Delta t_{MD}) - \boldsymbol{r}_j(t + \Delta t_{MD}), \tag{12}$$

$$\boldsymbol{v}_{ij}(t + \Delta t_{MD}) = \boldsymbol{v}_i(t + \Delta t_{MD}) - \boldsymbol{v}_j(t + \Delta t_{MD}), \tag{13}$$

And the specific form of the variables related to the Coulomb's friction in the simulation is given as:

$$\boldsymbol{e}_{ij}(t + \Delta t_{MD}) = \boldsymbol{r}_{ij}(t + \Delta t_{MD})/|\boldsymbol{r}_{ij}(t + \Delta t_{MD})|, \tag{14}$$

$$\delta n_{ij}(t + \Delta t_{MD}) = \boldsymbol{r}_{ij}(t + \Delta t_{MD})\cdot\boldsymbol{e}_{ij}(t + \Delta t_{MD}), \tag{15}$$

$$\Delta\boldsymbol{s}_{ij}(t + \Delta t_{MD}) = \boldsymbol{r}_{ij}(t + \Delta t_{MD}) - \delta n_{ij}(t + \Delta t_{MD})\cdot\boldsymbol{e}_{ij}(t + \Delta t_{MD}), \tag{16}$$

$${\boldsymbol{v}_{ij}}^{\mathrm{T}}(t + \Delta t_{MD}) = \boldsymbol{e}_{ij}(t + \Delta t_{MD})\times\boldsymbol{v}_{ij}(t + \Delta t_{MD})\times\boldsymbol{e}_{ij}(t + \Delta t_{MD}), \tag{17}$$

If the contact forces fulfill the Coulomb's friction law ($|{\boldsymbol{F}_{T,ij}}^{Contact}| \leqslant \mu|{\boldsymbol{F}_{N,ij}}^{Contact}|$), then the real tangential displacement between particles ${\Delta\boldsymbol{s}_{ij}}^{r}(t + \Delta t_{MD})$ is equal to the theoretical value $\Delta\boldsymbol{s}_{ij}(t + \Delta t_{MD})$; otherwise, when $|{\boldsymbol{F}_{T,ij}}^{Contact}|$ is larger than $\mu|{\boldsymbol{F}_{N,ij}}^{Contact}|$, the tangential displacement is obtained by: $\Delta{\boldsymbol{s}_{ij}}^{r}(t + \Delta t_{MD}) = \frac{\mu}{k_t}|{\boldsymbol{F}_{N,ij}}^{Contact}|\cdot\frac{{\boldsymbol{v}_{ij}}^{\mathrm{T}}}{|{\boldsymbol{v}_{ij}}^{\mathrm{T}}|}$. The final position $\boldsymbol{r}_i^f$ and velocity $\boldsymbol{v}_i^f$ of the colloidal particles are both dependent on the real tangential displacement, and shown as follows:

$$\boldsymbol{r}_i^f(t + \Delta t_{MD}) = \sum_{j\neq i}[\delta n_{ij}(t + \Delta t_{MD})\cdot\boldsymbol{e}_{ij}(t + \Delta t_{MD}) + \Delta\boldsymbol{s}_{ij}^{r}(t + \Delta t_{MD})] \tag{18}$$

$$\boldsymbol{v}_i^f(t + \Delta t_{MD}) = \boldsymbol{v}_i(t + \Delta t_{MD}) - \sum_{j\neq i}\boldsymbol{v}_{ij}(t + \Delta t_{MD})\left(1 - \frac{|\Delta{\boldsymbol{s}_{ij}}^{r}(t + \Delta t_{MD})|}{|\Delta\boldsymbol{s}_{ij}(t + \Delta t_{MD})|}\right). \tag{19}$$

2.2. Computational model details

The solvent particles in our simulation systems are taken as beads with a hard core of diameter d_S, which is set as 1% of the cutoff radius of solvent–solvent interactions r_{cut}, 75 nm. And the mass of solvent particles m_s is set as 1.99×10^{-18} kg. The conservative parameter a_{ij}, and dissipative parameter γ_{ij} for the solvent particles are chosen as 1.35×10^{-12} N, 6.03×10^{-9} N s m^{-1}, respectively. These solvent particles with highly small cores contribute less to the frictional interactions in the mesoscale system. The diameter

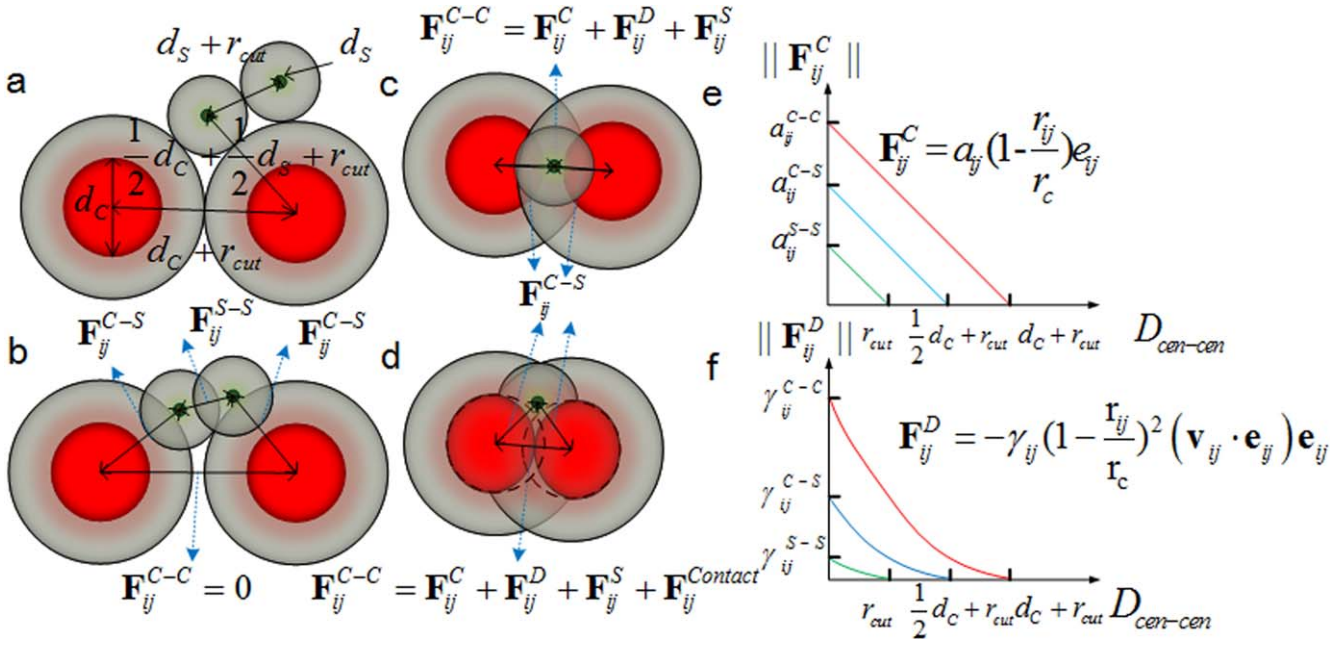

Figure 1. The schematic diagrams of interactions between different particles in colloidal suspension. The specific values of cut-off distances, r_c, between different particles are plotted in (a). The forces between different colloidal partices with different center-to-center distances are illustrated at, (a) $r_{ij} = r_c$, (b) $r_{contact} = d_c + d_S < r_c < r_{ij}$ (far from contact), (c) $d_c + d_S \leqslant r_{ij} < r_c$ (near contact), and (d) $r_{ij} < d_c + d_S$ (contact). The conservative and dissipative forces between different types of particles are drawn in (e), and (f), respectively.

of colloidal particles is denoted as $D = 300$ nm. The mass of colloidal particles is calculated from: $m_c = (D/r_{cut} + 1)^3 m_s$. The tangential elasticity constants k_t is set as 72 N m^{-1}, and the normal elasticity constants is taken as $k_n = 144$ N m^{-1} in the simulation. The frictional coefficient μ is selected as 1.0. The conservative parameter a_{ij} and dissipative parameter γ_{ij} between different particles are dependent on the size of colloidal particles.

As is plotted in figure 1, the superscript *C–C, S–S,* and *C–S* are adopted to denote the interaction between the colloidal and colloidal particle, solvent and solvent particle, and colloidal and solvent particle, respectively:

$$\begin{cases} \dfrac{a_{ij}^{C-C}}{a_{ij}^{S-S}} = \dfrac{d_c}{r_{cut}} + 1, \quad \dfrac{a_{ij}^{C-S}}{a_{ij}^{S-S}} = \dfrac{d_c}{2r_{cut}} + 1 \\ \dfrac{\gamma_{ij}^{C-C}}{\gamma_{ij}^{S-S}} = \left(\dfrac{d_c}{r_{cut}} + 1\right)^2, \quad \dfrac{\gamma_{ij}^{C-S}}{\gamma_{ij}^{S-S}} = \left(\dfrac{d_c}{2r_{cut}} + 1\right)^2, \end{cases} \tag{20}$$

The interaction between different particles in the simulation system is very complex. To reduce the computation cost, the cut-off distance between different particles is chosen as plotted in figure 1(a). When the interparticle separation r_{ij} is larger than the cut-off distance, the interaction between different particles is zero. When $d_c + d_S < r_c^{C-C} < r_{ij}$, the interactions between colloidal particles F_{ij}^{C-C} is zero. If the separation distance r_{ij} between colloidal-solvent and solvent–solvent is smaller than the cut-off distance r_c^{C-S} and r_c^{C-S}, the interactions F_{ij}^{C-S} and F_{ij}^{S-S} are considered in the simulation process (figure 1(b)). When the distance between colloidal particles is smaller than the r_c^{C-C}: $d_c + d_S \leqslant r_{ij} < r_c^{C-C}$ (figure 1(c)), the interaction between the pair of colloidal particles F_{ij}^{C-C} is included in the simulation. In the Hooke-core model, if the distance between solute particles is smaller than $d_c + d_S$, the contact force start to take effect in the computation of interaction between the colloid–colloid particles, as shown in figure 1(d).

The simulation box is a cube with an edge length of $L_x = L_y = L_z = 2.25$ μm. The Lees–Edwards boundary condition [58, 59] is applied in the simulations. The total number of all DPD particles, including both solvent and dispersed ones, is 81 000. The volume fraction of colloidal particles is defined as: $\phi = N\pi D^3/6L_xL_yL_z$, where N is 450, the total number of colloidal particles. The temperature of the whole system is kept at 293 K. The time scale is denoted as: $\tau_0 = \sqrt{m_s {r_{cut}}^2/K_BT} = 1.86 \times 10^{-3}$ s, and the time step of this simulation is set as $\Delta t_{MD} = 186$ ps.

Two different external loading conditions are applied to the simulation system. Firstly, a steady simple shear deformation is exerted on the system for about 3×10^5 time steps. The apparent viscosity is calculated through the equation: $\eta = \tau_{xy}/\dot{\gamma}$, where τ_{xy} denotes the virial shear stress, which is obtained as an average value every 1000 steps, and $\dot{\gamma}$ denotes the applied shear rate [58]. The shear rate $\dot{\gamma}$, at which simple shear keeps, is consistent with the result calculated from the velocity gradient: dv/dl_y. Secondly, an oscillatory shear deformation is mimicked to study dynamic responce of the system. The applied shear strain is denoted as: $\gamma = \gamma_0 \sin(\omega t)$, in which ω and γ_0 are the angle frequency and strain amplitude of oscillatory shear, respectively. The complex viscosity is obtained by: $\eta^* = \frac{\sigma_0}{\omega\gamma_0}$, where σ_0 is the shear stress amplitude during the oscillation. And the storage

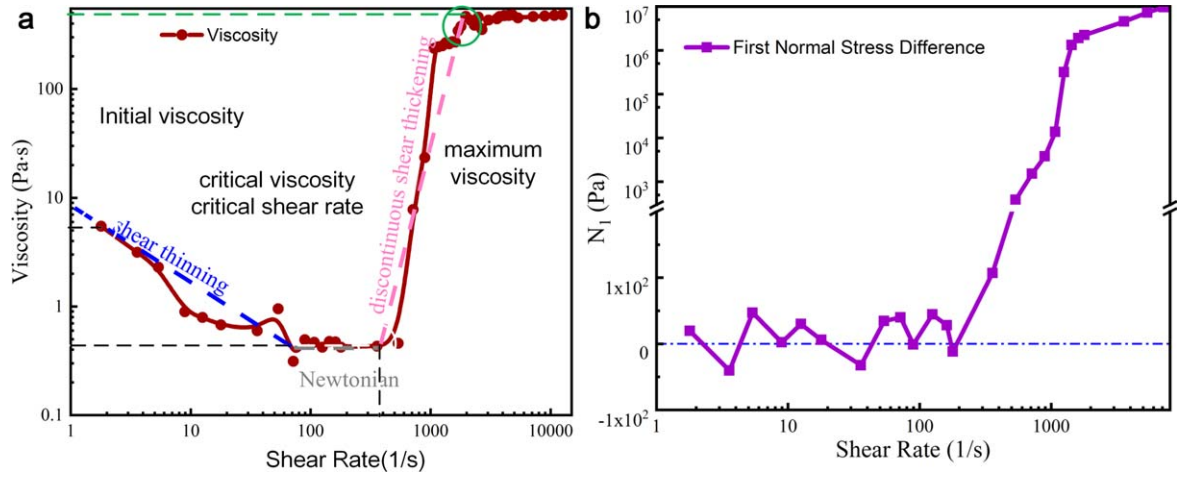

Figure 2. (a) Viscosity versus the shear rate in a typical DST suspension. (b) The first normal stress difference of the colloidal suspension under different shear rates.

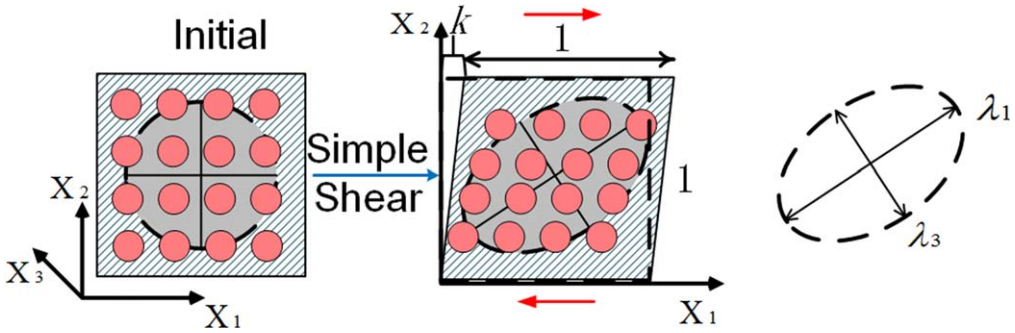

Figure 3. Illustration of simple shear deformation.

modulus and loss modulus are calculated from: $G' = \frac{\sigma_0}{\gamma_0}\cos\varphi$, $G'' = \frac{\sigma_0}{\gamma_0}\sin\varphi$, respectively.

3. Results and discussion

3.1. Typical DST phenomenon in steady shear deformation

The demonstration of simple shear under different shear rates is conducted. As shown in figure 2(a), the apparent viscosity at the shear rate of 1.79 s^{-1} is 5.46 Pa s. As the shear rate increases, the viscosity decreases firstly and then reaches a platform with an average value of 0.4 Pa s at the shear rate of 71.6 s^{-1}. And then, a sharp increase in viscosity emerges at the shear rate of 537 s^{-1}. After that, the viscosity starts to burst and reaches the highest value 482 Pa s at a shear rate of 1790 s^{-1}, which appears an obvious DST phenomenon. As can be seen in figure 2(a), the ST ratio of maximum/critical viscosity is about 1000, similar to the experimental results [59]. The relation between the first normal stress difference N_1 and the shear rate is plotted in figure 2(b). The first normal stress difference is defined as $N_1 = \sigma_{11} - \sigma_{22}$, where σ_{11} and σ_{22} are the stress components along the shear direction and normal to the shear plane, respectively. It is obvious that N_1 is fluctuating around zero before the critical shear rate. And with the suspension entering into the DST status, the N_1 starts to grow exponentially with the increase of shear rate, which means the elasticity of the suspension significantly increase with the shear rate increasing.

By considering a rectangular region in the simulation box, as illustrated in figure 3. If the region deforms under simple shear, the changed configuration as a function of the reference one is written as:

$$x_1 = X_1 + kX_2\ ;\ x_2 = X_2;\ x_3 = X_3, \tag{21}$$

where k is the amount of shear.

The relations between principal stretches λ_1, principal compression λ_3, and amount of shear, considering a plane strain state, i.e. $\lambda_2 = 1$, may be given by:

$$\lambda_1 = \sqrt{1 + \frac{k^2}{2} + k\sqrt{1 + \frac{k^2}{4}}} \text{ and } \lambda_3 = \sqrt{1 + \frac{k^2}{2} - k\sqrt{1 + \frac{k^2}{4}}}, \tag{22}$$

And thus, the distance between the colloidal particles in the rectangular region may increase along the principal stretches direction, but reduce along the principal compression direction.

The evolution of the radial distribution function (RDF) under different shear rates is analyzed. As plotted in figure 4(a), it shows that the first peak maintains steady before

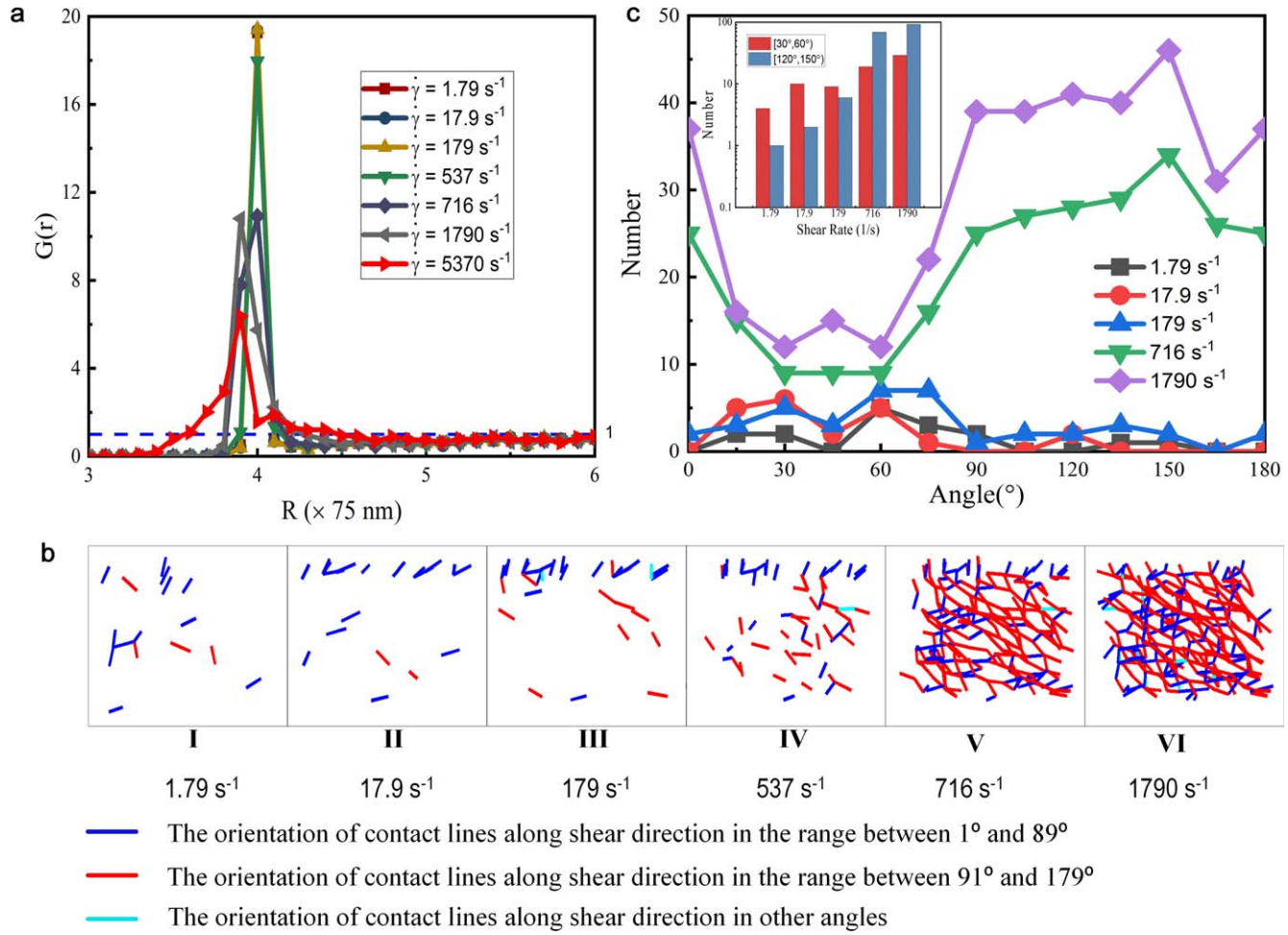

Figure 4. (a) The radial distribution function for colloidal particles at different shear rates in a typical DST suspension. (b) The illustration of contacts between contacted colloidal particles in the suspension under the increasing shear rate. The orientation of blue contact lines are in angle between 1° and 89°, the orientation of red contact lines are in angle between 91° and 179°, and the orientation of cyan contact lines are along others. (c) The number of particle contact along different angles with different shear rates. The insert shows the specific number of contacts along the directions of compression and stretching at different shear rates.

the shear rate of 537 s^{-1}. After that, with the shear rate increasing, the maximum of the peak reduces and the width increases. And it is found that the peak gradually shifts left after the critical shear rate, which means that the colloidal particles turn to be more compact during the ST process.

Here, the contact line method is used to trace the contact status between different colloidal particles. As the modified DPD method discussed, colloidal particles contact with each other when their mutual distance is smaller than $d_c + d_S$, a contact line is drawn between these two particles, and different colors are used to represent the contact orientation. If the orientation is in the range between 1° and 89°, it is painted in blue color. And if the orientation is in the range between 91° and 179°, it is colored in red. Others (horizontal and vertical orientation) are in cyan color. The contact lines under different shear rates are plotted in figure 4(b). It is found that few contact is emerged at lower shear rates. When the DST happens, the contact lines turn to be intensive and a stable contact network is formed. As it also can be seen from the figure 4(c), the contact along the principal compression direction suddenly increase when the shear rate exceed the critical shear rate. The compression contact makes the colloidal particles closer, which induces the left shift of the first peak in the RDF.

3.2. Dynamic mechanics analysis of the suspension

Besides the steady shear, a further numerical simulation is performed to study the formation of the contact network by using an oscillatory shear with different excitation frequencies. The variation of the complex viscosity with the frequency is analyzed and shown in figure 5(a). It is found that the complex viscosity shares the same critical shear rate with the ST behavior under steady shear deformation (figure 2(a)), which meets Cox–Merz rule [60] very well. The changes of storage and loss modulus with the excitation frequency in the simulation are also plotted in figure 5(b). The two moduli both raise with the increase of frequency, and the increase ratio of storage modulus is much higher than that of loss one, which displays the rapid transition from viscosity to elasticity of the whole colloidal suspension after the critical shear rate. By calculating the variation of phase angle with the

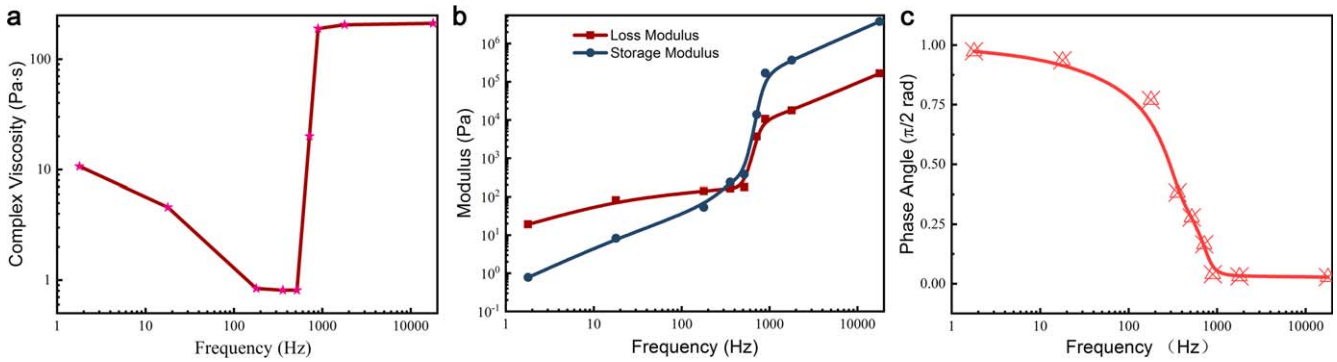

Figure 5. (a) The complex viscosity versus frequency in the colloidal suspension. (b) The storage and loss modulus along the frequency of suspension in the simulation. (c) The phase angle between shear strain and stress as a function of frequency.

frequency in figure 5(c), it can further illustrate the transition from viscosity ($\varphi = \frac{\pi}{2}$) to elasticity ($\varphi = 0$) by the ST behavior.

The evolution of friction contact network during the oscillation with a 716 Hz excitation frequency is also investigated. As illustrated in figure 6(a), the snapshots of contact lines in the suspension system at different time points are provided, and the contact numbers at each time point count up in figure 6(b). It shows that the frictional contact network has an obvious periodic trend. When the shear strain is zero (time point I and V), the number density of the contact network reaches maximum due to the largest shear rate. After that, the density of the contact network gradually reduces until the shear direction changes (II, VI and VII). With the shear direction reversing (III and VIII), few contacts happen. And then, with the shear strain reduced, the contact network emerges again. It is seen that most of the contact direction is along the compression direction in the simple shear deformation. Under the oscillatory shear deformation, the formation time of the contact network is closely related to the excited frequency. Under lower excited frequencies, there is no contact network formed as only shear-thinning phenomenon happens. While under higher excited frequencies, the contact network suddenly appears. The number of 140 is chosen as the monitoring value for the formation of the contact network. Here T is one cycle time period of the shear deformation. The variation of formation time with excited frequency is shown in figure 6(c). It is found that at the low shear frequency, there is no contact network. At the shear frequency of 537 Hz, the contact network starts to appear. Then with the loading frequency increasing, the formation time for the contact network is reduced. From the simulation results under oscillatory shear, it is confirmed that the formation of the contact network between colloidal particles is the key factor for the DST behaviors of densified suspensions.

3.3. EVF during DST

The viscosity of the monodisperse suspension can be calculated by a general function $\eta_r = f(\phi, Pe_{\dot{\gamma}}, Re_{\dot{\gamma}})$, where η_r is the relative viscosity of the suspension ($\eta_r = \eta/\eta_0$, where η_0 denotes the viscosity of the pure solvent), ϕ is the volume fraction and $Pe_{\dot{\gamma}}$, $Re_{\dot{\gamma}}$ are both regarded as invariants number when the shear rate is fixed [61]. Therefore, the viscosity is determined by the volume fraction. During the DST stage in both of the steady and dynamic shear, the interparticle frictional contact accelerates the solidification from the point of the whole suspension. Besides, from the perspective of a single particle, the solvent particles are squeezed out under the action of the frictional contact of elastic cores. As the contact network formed, the solvent particles locked in the center of the colloidal particles network, which can be described as the 'restrained solvent particles', contribute little to the lubrication and friction in the suspension. These restricted solvent particles are seen to fill the blank areas in the cube, which is around the contact area between each pair of colloidal particles. Meanwhile, the solvent particles surrounding the colloidal particles are regarded as the 'free solvent particles', which can flow freely in the suspension. The total volume of colloidal particles and restrained solvent particles are the effective volume that affects the ST behavior. The expression of the EVF is as follows:

$$\phi_e = \frac{V_{cp} + V_{rs}}{V} = \frac{V_{cp} + V_{rs}}{V_{cp} + V_{fs} + V_{rs}}, \tag{23}$$

where ϕ_e is the EVF, V_{cp}, V_{rs} and V_{fs} are the volume of colloidal particles, the restrained solvent particles, and the free solvent particles, respectively. As the figure 7(a) shows, the colloidal particles are thus split into two parts, the contact ones, and the individual ones:

$$V_{cp} = V_{con} + V_{ind}, \tag{24}$$

where V_{con} denotes the volume of contact particles, and the V_{ind} denotes that do not contact.

For the V_{ind}, the formula for the volume fraction is:

$$V_{ind} = Q\pi D^3/6, \tag{25}$$

where Q is the total number of individual colloidal particles, D is the diameter of colloidal particles.

When the colloidal particles contact, the Hooke-core deforms because of the normal contact force, leading to an

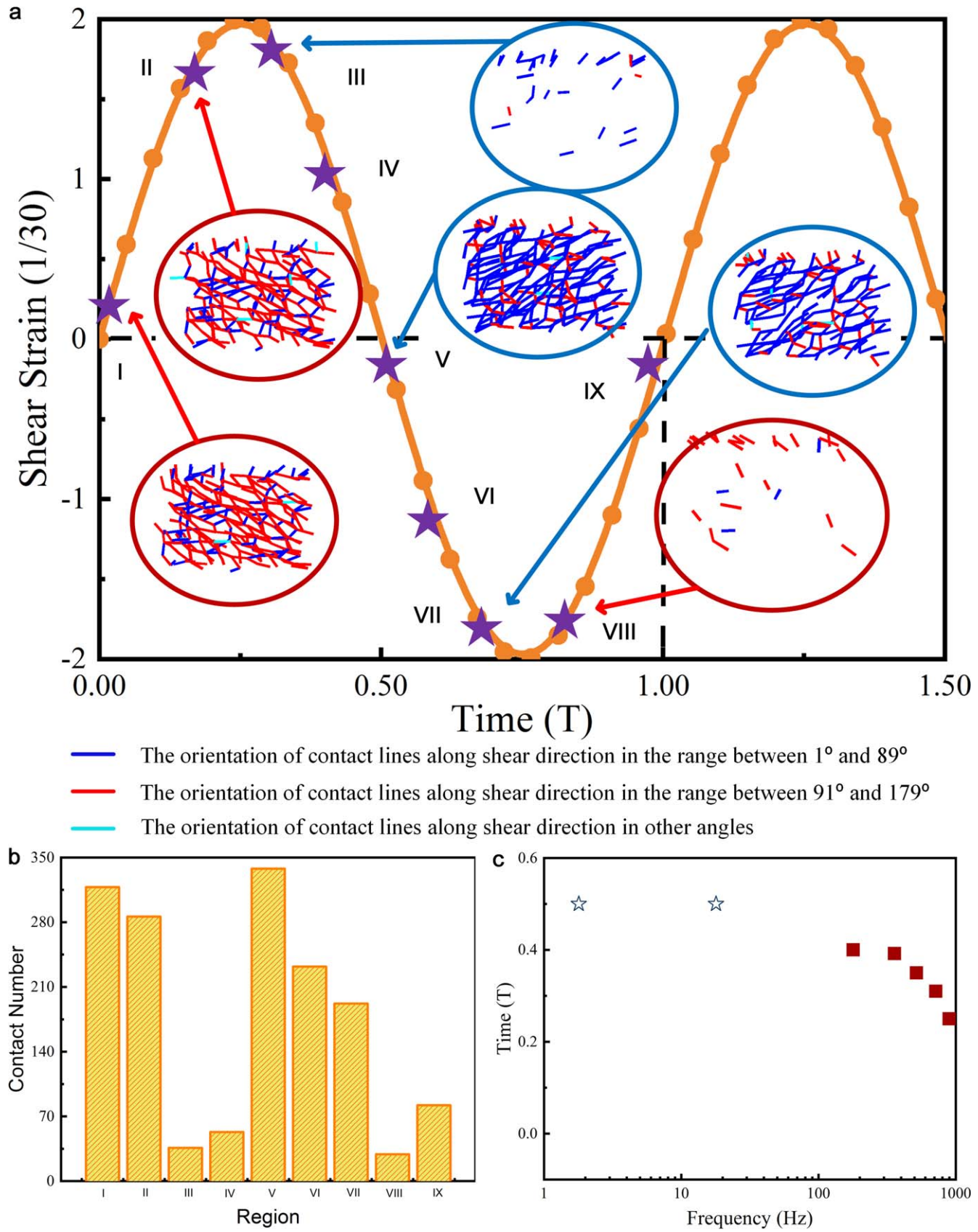

Figure 6. (a) The shear strain over time of the suspension under oscillatory shear at a frequency of 716 Hz. The insert shows the snapshots of colloidal particle microstructure under medium frequency oscillatory shear at the different shear time points. The orientation of blue contact lines are in angle between 1° and 89°, the orientation of red contact lines are in angle between 91° and 179°, and the orientation of cyan contact lines are along others. (b) The histogram of particle contact number in the nine shear points of the insert in (a). (c) The formation time of particle contact network in each cycle T.

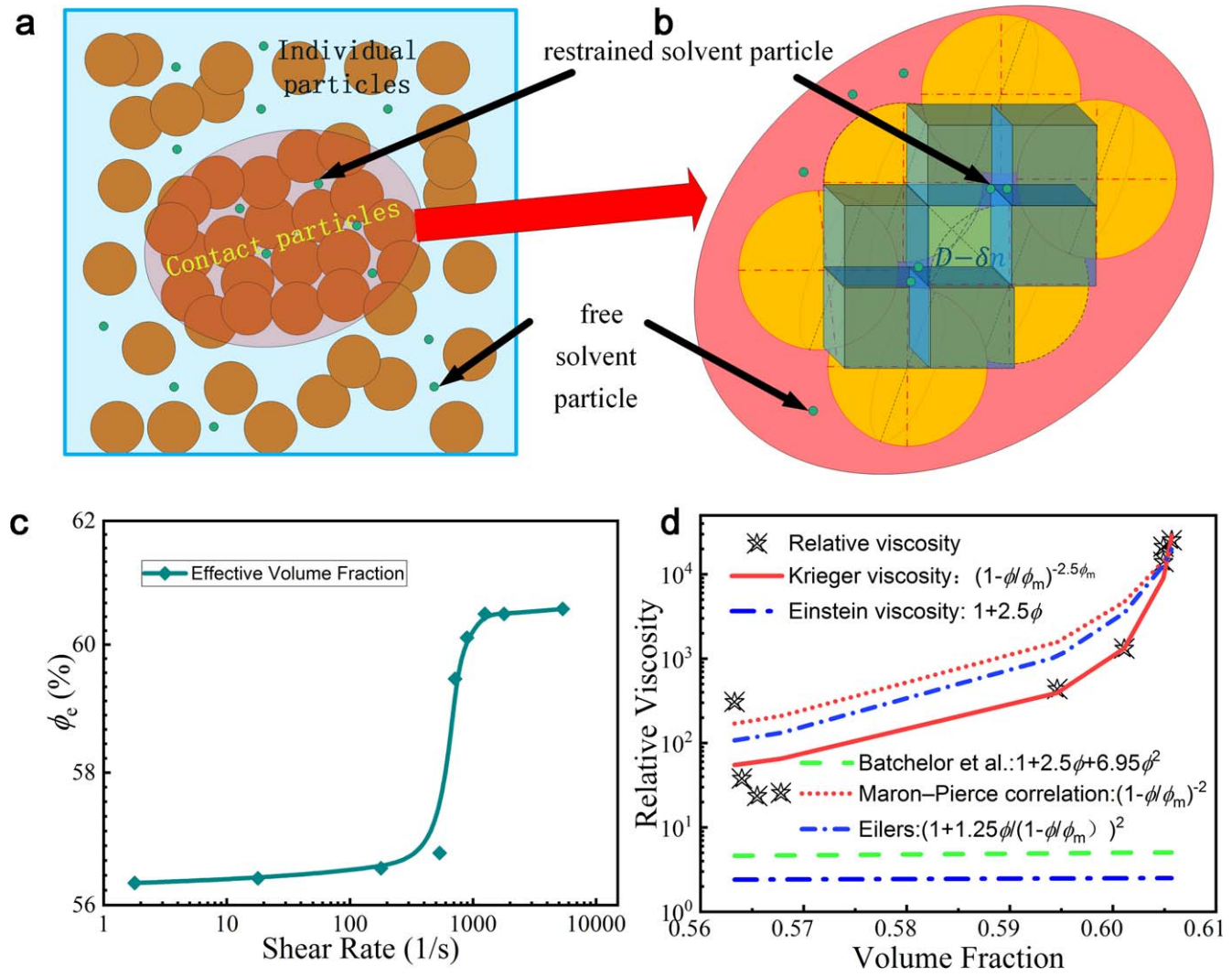

Figure 7. (a) Schematic illustration of the particles during the DST process. (b) The illustration of the effective volume of colloidal particles at contact. (c) The effective volume fraction as a function of the shear rate. (d) The fitted curves of the relative viscosity versus EVF in suspensions.

error of $o(\delta n^3)$ in the calculation of the volume of colloidal particles. The volume of the contact particles in the system is as follows:

$$V_{con} = \frac{1}{6}(N - Q)\pi D^3 + o(\delta n^3), \tag{26}$$

where N is the total number of the colloidal particles, and $o(\delta n^3)$ denotes the slight deformation of the contacted particles.

Along the inter-particle core-to-core distance of contacted particles, a cube is adopted with a diagonal length of $(D - \delta n)$. Thus, $1/8$ part of the sphere in each core is included in the new cube with side length of $(D - \delta n)/\sqrt{3}$, which is obvious in figure 7(b). The deformed cores occupy the overlap area of cores and cube, while the squeezed-out solvent particles fill the blank are of the cube. The volume of the restrained solvent particles at each contact is given as:

$$V_{rs} = V_{cube} - \frac{1}{4}V_{sphere} = \frac{1}{3\sqrt{3}}(D - \delta n)^3 - \frac{\pi}{24}D^3, \tag{27}$$

where V_{cube} is the volume of the cube region, and V_{sphere} denotes the volume of each colloidal particle.

Finally, the EVF of colloidal particles, induced by the deformed colloidal particles and the packaged solvent particles, is a function of the contact number m:

$$\phi_e = \left\{\frac{1}{6}N\pi D^3 + \sum_1^m\left[\frac{1}{3\sqrt{3}}(D - \delta n)^3 - \frac{\pi}{24}D^3\right] + o(\delta n^3)\right\}/L^3. \tag{28}$$

The changes of EVF along the shear rate is plotted in figure 7(c).

A relative viscosity expression is adopted here same as the Krieger viscosity [61, 62] formulation:

$$\eta_r = (1 - \phi_e/\phi_m)^{-2.5\phi_m}. \tag{29}$$

where ϕ_e is the EVF, ϕ_m is the maximum volume fraction, for which the suspensions cease to flow [61]. The variation of the relative viscosity is fitted and the result comparing with other equations is shown in figure 7(d). It is obvious that the

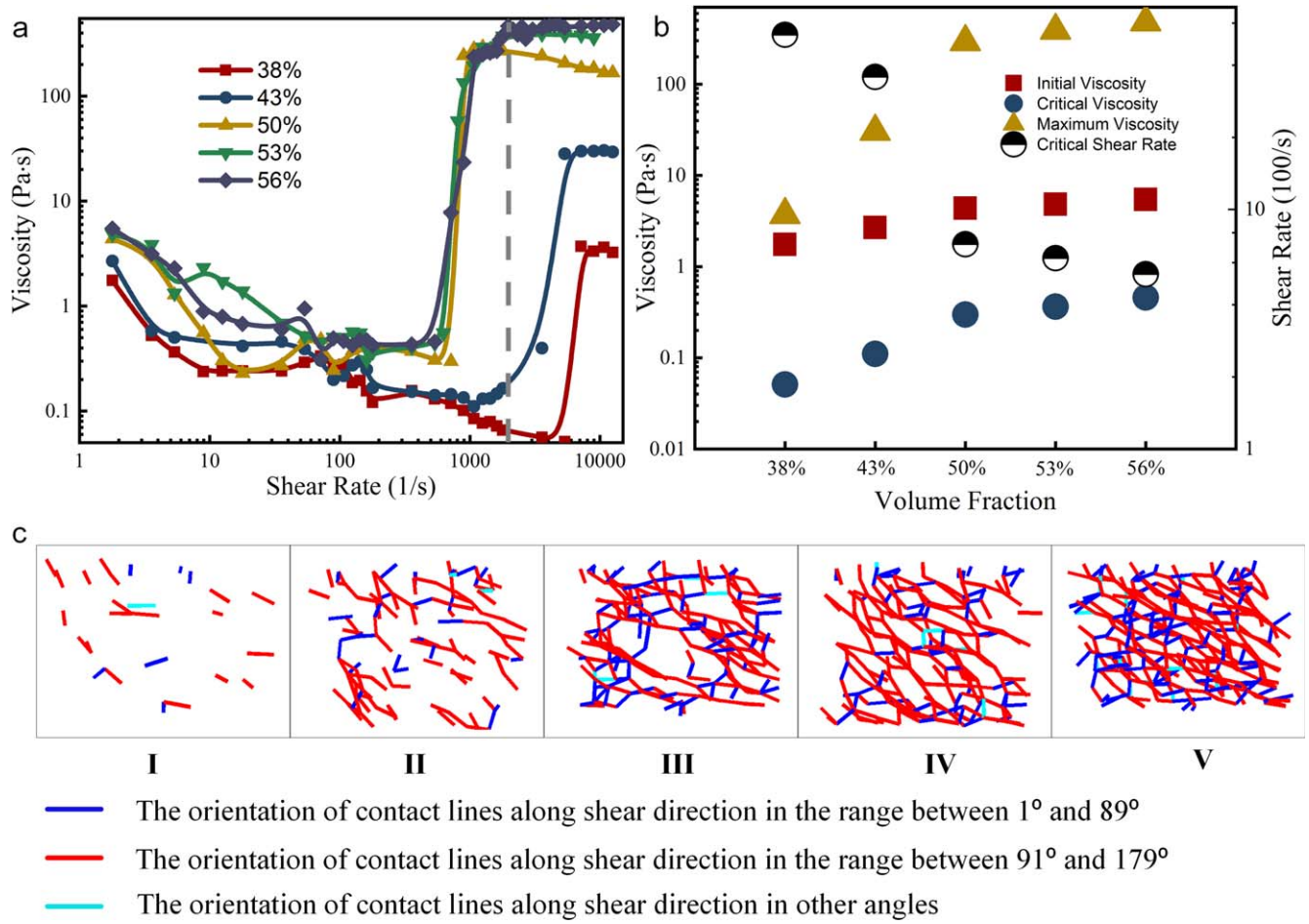

Figure 8. (a) The viscosity versus shear rate of colloidal suspensions with different phase volume fractions. (b) The initial, the critical, and the maximum viscosity, as well as the critical shear rate in ST phenomenon as a function of different volume fractions. (c) The snapshots of particle contact of suspensions with different volume fraction at a shear rate of 1790 s^{-1}. The orientation of blue contact lines are in angle between 1° and 89°, the orientation of red contact lines are in angle between 91° and 179°, and the orientation of cyan contact lines are along others. (I) 38% vol. (II) 43% vol. (III) 50% vol. (IV) 53% vol. (V) 56% vol.

viscosity model defined by the EVF, which is based on the frication contact network, can effectively describe the discontinuous shear thickening behaviors.

4. Influence factors of suspension on DST behavior

4.1. Volume fraction of colloidal particles

As reported in previous literature [19–22], the volume fractions would affect the ST behavior. Here we set up several different systems in which the volume fraction ϕ of colloidal particles is about 38%, 43%, 50%, 53%, 56%, respectively. And other parameters are the same as those defined in the system A. As shown in figure 8(a), the typical DST phenomenon is emerged in each system. According to the results, it can be found that there is a positive correlation between the volume fraction and the initial viscosity (figure 8(b)). Conversely, the development of the critical viscosity shows a reverse trend. The evolution of contact status between different colloidal particles is provided in figure 8(c). As can be seen, the formation of the contact network is more easy in the suspensions with higher volume fraction. The EVF of low concentration is obviously low than that of high one, no matter at the beginning stage or the DST period. As a result, the system with a higher volume fraction have a higher maximum viscosity and can enter into the DST status at a smaller critical shear rate.

4.2. Particle size of colloidal particles

To understand the effect of the particle size on the DST effects, another simulation is carried out by setting the colloidal particle diameter d_c as 240 nm, 270 nm, 300 nm, 330 nm, 360 nm, respectively. The number of colloidal particles varies to maintain the volume fraction constant at 56%. The other parameters are the same as which defined in the system A. Figure 9(a) displays the apparent viscosities of all the systems with different particle diameters under steady shear. Although the number density for small colloidal particles is large, the contact interaction between colloidal particles and the hydrodynamics interaction with surrounding solvent particles do not increase as much, due to the small action area in each small particle at the stage of entering DST.

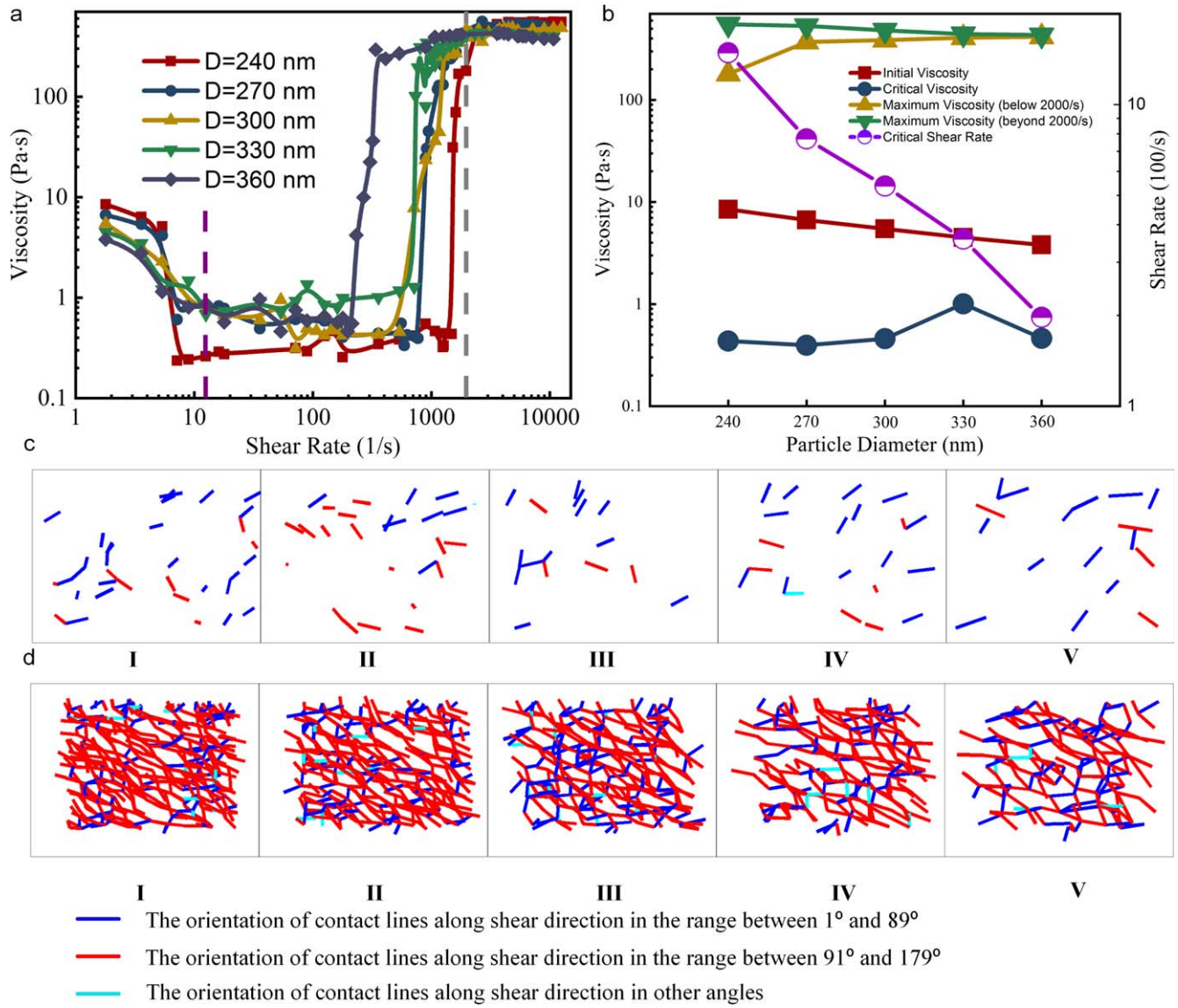

Figure 9. (a) The viscosity versus shear rate of colloidal suspensions with different colloidal particle diameters. (b) Several viscosities and the critical shear rate in ST as functions of particle diameters. (c) The snapshots of particle contact of different suspensions at the initial shear rate of 1.79 s^{-1}. (d) The snapshots of particle contact of suspensions at a shear rate of 1790 s^{-1}. The orientation of blue contact lines are in angle between 1° and 89°, the orientation of red contact lines are in angle between 91° and 179°, and the orientation of cyan contact lines are along others. (I) $d_c = 240$ nm. (II) $d_c = 270$ nm. (III) $d_c = 300$ nm. (IV) $d_c = 330$ nm. (V) $d_c = 360$ nm.

As a result, the initial viscosity and the maximum viscosity show slightly decline with the shear rate increasing, as shown in figure 9(b). On the other hand, from point of the evolution in figures 9(c) and (d), due to the low increase of EVF in the suspension with small colloidal particles, it needs a higher shear rate to form the stable contact network for the DST phenomenon emergence. Our simulation results fit very well with Kalman's experiment results [21].

4.3. Particle surface roughness of colloidal particles

The influence of the particles surface roughness on the DST behavior is also studied here by changing the friction coefficient μ of colloidal particles. Figure 10(a) presents the curves of apparent viscosity versus shear rate of suspensions with different friction coefficients. It clearly shows that there is no obvious DST phenomenon when the friction coefficient μ is below 0.6. Though the viscosity in suspension with particle friction coefficient of 0.4 raises a little at a very high shear rate, this curve shows no DST effect because of the initial viscosity far larger than the final one. Therefore, we define 0.6 as the critical friction coefficient for the DST behavior in current suspension system, below which the DST does not appear. From figure 10(b), it can be concluded that there is a smaller critical shear rate, a higher initial viscosity, a higher critical viscosity, and a higher maximum viscosity in the system with higher particle roughness. Further simulations are conducted to explore the relationship between the critical friction coefficient and the volume fraction of colloidal particles. The reduction of critical friction coefficient accompanied with the increasement of the contents of colloidal particles is plotted in figure 10(c). It can be found that more

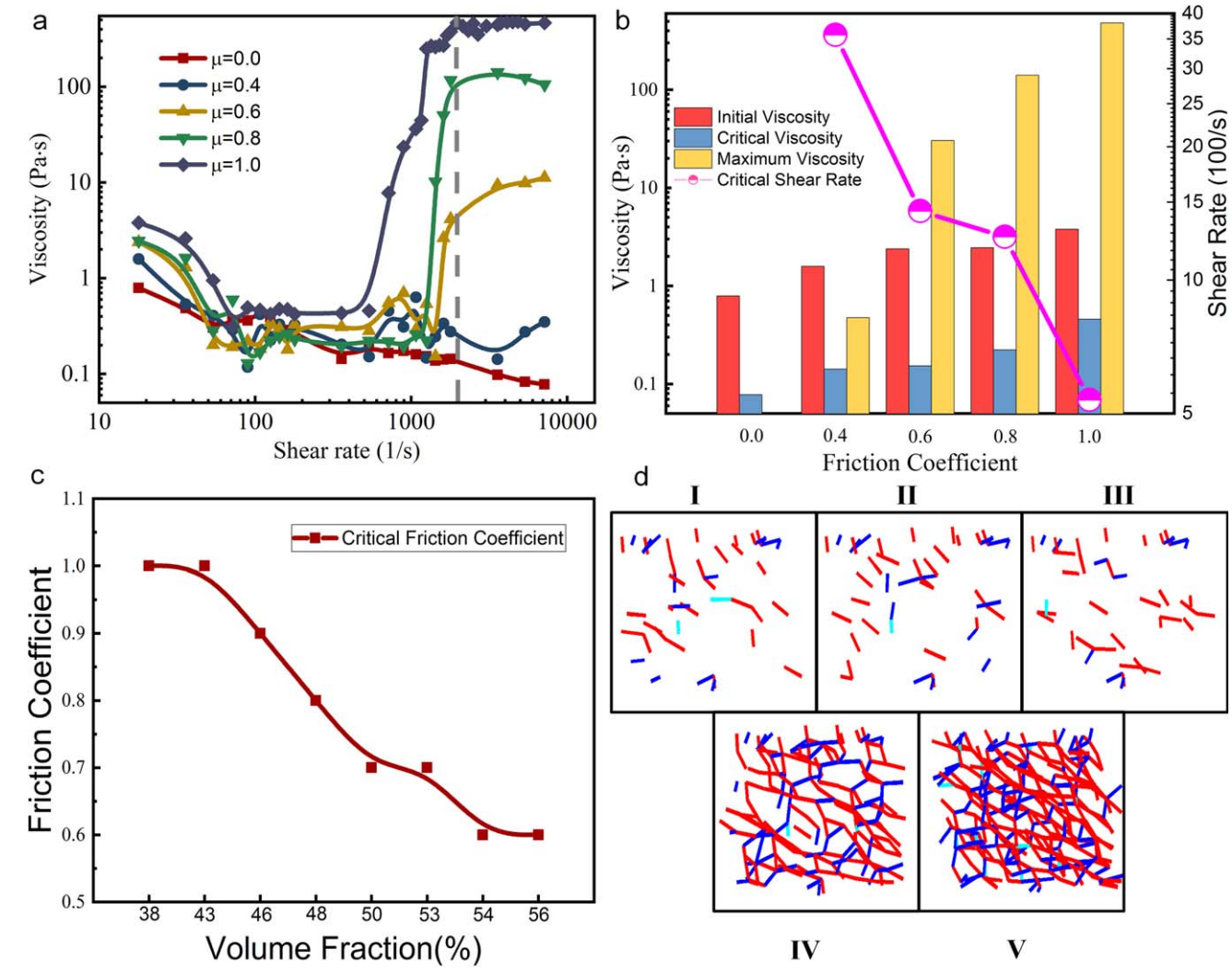

Figure 10. (a) Shear rate dependence of viscosity with different particle surface roughness. (b) The initial, the minimum, and the maximum viscosity, as well as critical shear rate in ST dependence of particle surface friction coefficient. (c) The relationship between critical friction coefficient and the content of colloidal particles connected with the occurance of DST behaviors. (d) The snapshots of particle contact of suspensions with different particle friction coefficient at a shear rate of 1790 s^{-1}. The orientation of blue contact lines are in angle between 1° and 89°, the orientation of red contact lines are in angle between 91° and 179°, and the orientation of cyan contact lines are along others. (I) $\mu = 0.0$. (II) $\mu = 0.4$. (III) $\mu = 0.6$. (IV) $\mu = 0.8$. (V) $\mu = 1.0$.

rough surface of the colloidal would do help to the occurrence of DST behavior in suspension with lower colloidal concentration. As reported in Hsiao's work [29], it is found that the smooth colloidal particles can minimize ST behavior, which is consistent very well with our results. As for the evolution of contact networks in figure 10(d), obviously, since the high tangential contact interaction can be more beneficial to impede the movement of a colloidal particle under hydrodynamics interaction, it is easy for the suspension with rougher colloidal particles to form a stable contact network. Thus, the EVF in suspension with smooth particles is small, comparing to that with rough particles. From this point of view, it can be confirmed that the frictional contact interaction between different colloidal particles takes the key role in the formation of a stable contact network, which is the cause of the appearance of the DST phenomenon.

5. Conclusions

On the basis of the reported approaches [34, 54–58], the core-modified DPD mesoscale method is adopted to study the non-Newtonian behavior of STFs. Both steady and oscillatory shear actions are taken to study the rheological properties of the suspension, as well as the static and dynamic response of the system. It is proved successively that the shift of viscosity

is firmly connected with that of frictional contact network. The rheological properties and microstructural evolution of the suspensions with different influence factors are also investigated. A relationship is established between the relative viscosity and the EVF during DST. We have obtained good agreements between our simulation results and the real experimental data [21, 29].

Under the shear action, the dominated inter-particle interaction in suspension is determined by the competition between hydrodynamics and frictional contact force. This transition leads to the rivalry between formation and destruction of frictional contact networks in microscale. The particle contact also induces the increase of the EVF of the colloidal particle in the STF. In macroscale, the viscosity of the system raises dramatically with shear rate during the DST process. This correspondence, throughout local and global of the system, between microstructure and viscosity under shear in STF is consistent well with previous findings [17–21, 34–38, 63–65].

This work can also predict some results, which are hardly obtained directly due to the limitations of the existing experimental conditions. These findings can also provide guidance for preparing STFs that meet specific engineering requirements.

Acknowledgments

Financial supports from the National Natural Science Foundation of China (Grant No. 11772320), the Strategic Priority Research Program of the Chinese Academy of Sciences (Grant No. XDB22040502), the fundamental research funds for the Central Universities (WK2480000002, WK2090050045), and the Opening Project of Applied Mechanics and Structure Safety Key Laboratory of Sichuan Province (SZDKF-1701) are gratefully acknowledged. This work is also supported by the Collaborative Innovation Center of Suzhou Nano Science and Technology.

ORCID iDs

Xinglong Gong https://orcid.org/0000-0001-6997-9526

Reference

[1] Tian T and Nakano M 2017 Design and testing of a rotational brake with shear thickening fluids *Smart Mater. Struct.* **26** 035038
[2] Wei M H, Hu G, Li L X and Liu H T 2018 Development and theoretically evaluation of an STF-SF isolator for seismic protection of structures *Meccanica* **53** 841–56
[3] Yang J, Sun S S, Li W H, Du H P, Alici G and Nakano M 2015 Development of a linear damper working with magnetorheological shear thickening fluids *J. Intell. Mater. Syst. Struct.* **26** 1811–7
[4] Zhou Z, Hollingsworth J V, Hong S, Wei G M, Shi Y, Lu X, Cheng H and Han C C 2014 Effects of particle softness on shear thickening of microgel suspensions *Soft Matter* **10** 6286–93
[5] Ness C and Sun J 2016 Shear thickening regimes of dense non-brownian suspensions *Soft Matter* **12** 914–24
[6] Pednekar S, Chun J and Morris J F 2017 Simulation of shear thickening in attractive colloidal suspensions *Soft Matter* **13** 1773–9
[7] Crawford N C, Popp L B, Johns K E, Caire L M, Peterson B N and Liberatore M W 2013 Shear thickening of corn starch suspensions: does concentration matter? *J. Colloid Interface Sci.* **396** 83–9
[8] Cwalina C D, Harrison K J and Wagner N J 2016 Rheology of cubic particles suspended in a Newtonian fluid *Soft Matter* **12** 4654–65
[9] Denn M M, Morris J F and Bonn D 2018 Shear thickening in concentrated suspensions of smooth spheres in Newtonian suspending fluids *Soft Matter* **14** 170–84
[10] Jamali S, Boromand A, Wagner N and Maia J 2015 Microstructure and rheology of soft to rigid shear-thickening colloidal suspensions *J. Rheol.* **59** 1377–95
[11] Jamali S, Yamanoi M and Maia J 2013 Bridging the gap between microstructure and macroscopic behavior of monodisperse and bimodal colloidal suspensions *Soft Matter* **9** 1506–15
[12] Speedy R J 1999 Glass transition in hard disc mixtures *J. Chem. Phys.* **110** 4559–65
[13] Marshall L and Zukoski C F 1990 Experimental studies on the rheology of hard-sphere suspensions near the glass-transition *J. Phys. Chem.* **94** 1164–71
[14] Maranzano B J and Wagner N J 2001 The effects of particle-size on reversible shear thickening of concentrated colloidal dispersions *J. Chem. Phys.* **114** 10514–27
[15] Hoogerbrugge P J and Koelman J M V A 1992 Simulating microscopic hydrodynamic phenomena with dissipative particle dynamics *Europhys. Lett.* **19** 155–60
[16] Hoffman R L 1974 Discontinuous and dilatant viscosity behavior in concentrated suspensions: II. Theory and experimental tests *J. Colloid Interface Sci.* **46** 491–506
[17] Hoffman R L 1998 Explanations for the cause of shear thickening in concentrated colloidal suspensions *J. Rheol.* **42** 111–23
[18] Maranzano B J and Wagner N J 2002 Flow-small angle neutron scattering measurements of colloidal dispersion microstructure evolution through the shear thickening transition *J. Chem. Phys.* **117** 10291–302
[19] Melrose J R and Ball R C 2004 Continuous shear thickening transitions in model concentrated colloids-the role of interparticle forces *J. Rheol.* **48** 937–60
[20] Gopalakrishnan V and Zukoski cf 2004 Effect of attractions on shear thickening in dense suspensions *J. Rheol.* **48** 1321–44
[21] Kalman D P and Wagner N J 2009 Microstructure of shear-thickening concentrated suspensions determined by flow-USANS *Rheol. Acta* **48** 897–908
[22] Cwalina C D and Wagner N J 2016 Rheology of non-brownian particles suspended in concentrated colloidal dispersions at low particle Reynolds number *J. Rheol.* **60** 47–59
[23] Cwalina C D and Wagner N J 2014 Material properties of the shear-thickened state in concentrated near hard-sphere colloidal dispersions *J. Rheol.* **58** 949–67
[24] Gurnon A K and Wagner N J 2015 Microstructure and rheology relationships for shear thickening colloidal dispersions *J. Fluid Mech.* **769** 242–76
[25] Khandavalli S and Rothstein J P 2015 Large amplitude oscillatory shear rheology of three different shear-thickening particle dispersions *Rheol. Acta* **54** 601–18
[26] Morris J F 2009 A review of microstructure in concentrated suspensions and its implications for rheology and bulk flow *Rheol. Acta* **48** 909–23

[27] Foss D R and Brady J F 2000 Structure, diffusion and rheology of brownian suspensions by stokesian dynamics simulation *J. Fluid Mech.* **407** 167–200
[28] Singh A, Mari R, Denn M M and Morris J F 2018 A constitutive model for simple shear of dense frictional suspensions *J. Rheol.* **62** 457–68
[29] Hsiao L C, Jamali S, Glynos E, Green P F, Larson R G and Solomon M J 2017 Rheological state diagrams for rough colloids in shear flow *Phys. Rev. Lett.* **119** 158001
[30] Mai-Duy N, Phan-Thien N and Khoo B C 2015 Investigation of particles size effects in Dissipative Particle Dynamics (DPD) modelling of colloidal suspensions *Comput. Phys. Commun.* **189** 37–46
[31] Chen K H, Wang Y, Xuan S H and Gong X L 2017 A hybrid molecular dynamics study on the non-Newtonian rheological behaviors of shear thickening fluid *J. Colloid Interface Sci.* **497** 378–84
[32] Jia W P, Shan L, Zhang W L, Meng Y G and Tian Y 2018 Scaling magneto-rheology based on Newtonian and non-Newtonian host fluids *Smart Mater. Struct.* **27** 105019
[33] Tan Z H, Li W H and Huang W 2018 The effect of graphene on the yarn pull-out force and ballistic performance of kevlar fabrics impregnated with shear thickening fluids *Smart Mater. Struct.* **27** 075048
[34] Peters I R, Majumdar S and Jaeger H M 2016 Direct observation of dynamic shear jamming in dense suspensions *Nature* **532** 214–7
[35] Malkin A Y and Kulichikhin V G 2016 Shear thickening and dynamic glass transition of concentrated suspensions. state of the problem *Colloid J.* **78** 1–8
[36] Mari R, Seto R, Morris J F and Denn M M 2014 Shear thickening, frictionless and frictional rheologies in non-Brownian suspensions *J. Rheol.* **58** 1693–724
[37] Laun H M 1984 Rheological properties of aqueous polymer dispersions *Angew. Makromol. Chem.* **123** 335–59
[38] Rathee V, Blair D L and Urbach J S 2017 Localized stress fluctuations drive shear thickening in dense suspensions *Proc. Natl Acad. Sci. USA* **114** 8740–5
[39] Townsend A K and Wilson H J 2017 Frictional shear thickening in suspensions: the effect of rigid asperities *Phys. Fluids* **29** 121607
[40] Mari R, Seto R, Morris J F and Denn M M 2015 Nonmonotonic flow curves of shear thickening suspensions *Phys. Rev.* E **91** 052302
[41] Jiang W, Xuan S and Gong X 2015 The role of shear in the transition from continuous shear thickening to discontinuous shear thickening *Appl. Phys. Lett.* **106** 151902
[42] Jiang W, Peng G, Ma Y, Chen H, Hu J, Jia C and Zhang T 2017 Measuring the mechanical responses of a jammed discontinuous shear-thickening fluid *Appl. Phys. Lett.* **111** 201906
[43] Faltas M S and El-Sapa S 2018 Rectilinear oscillations of two spherical particles embedded in an unbounded viscous fluid *Microsyst. Technol.* **25** 39–49
[44] Saad E I 2012 Motion of two spheres translating and rotating through a viscous fluid with slip surfaces *Fluid Dyn. Res.* **44** 055505
[45] El-Sapa S, Saad E I and Faltas M S 2018 Axisymmetric motion of two spherical particles in a Brinkman medium with slip surfaces *Eur. J. Mech.* B **67** 306–13
[46] Barnes H A 1989 Shear-Thickening (Dilatancy) in suspensions of nonaggregating solid particles dispersed in Newtonian liquids *J. Rheol.* **33** 329–66
[47] Maranzano B J and Wagner N J 2001 The effects of interparticle interactions and particle size on reversible shear thickening: hard-sphere colloidal dispersions *J. Rheol.* **45** 1205–22
[48] Asija N, Chouhan H, Gebremeskel S A and Bhatnagar N 2017 Influence of particle size on the low and high strain rate behavior of dense colloidal dispersions of nanosilica *J. Nanopart. Res.* **19** 21
[49] Brown E, Forman N A, Orellana C S, Zhang H J, Maynor B W, Betts D E, DeSimone J M and Jaeger H M 2010 Generality of shear thickening in dense suspensions *Nat. Mater.* **9** 220–4
[50] Maharjan R and Brown E 2017 Giant deviation of a relaxation time from generalized Newtonian theory in discontinuous shear thickening suspensions *Phys. Rev. Fluids.* **2** 123301
[51] Cwalina C D, Harrison K J and Wagner N J 2017 Rheology of cubic particles in a concentrated colloidal dispersion suspending medium *AIChE J.* **63** 1091–101
[52] Gao J S, Mwasame P M and Wagner N J 2017 Thermal rheology and microstructure of shear thickening suspensions of silica nanoparticles dispersed in the ionic liquid [C(4) mim][BF4] *J. Rheol.* **61** 525–35
[53] Yang W F, Wu Y, Pei X W, Zhou F and Xue Q J 2017 Contribution of surface Chemistry to the shear thickening of silica nanoparticle suspensions *Langmuir* **33** 1037–42
[54] Groot R D and Warren P B 1997 Dissipative particle dynamics: Bridging the gap between atomistic and mesoscopic simulation *J. Chem. Phys.* **107** 4423–35
[55] Espanol P and Warren P 1995 Statistical-Mechanics of dissipative particle dynamics *Europhys. Lett.* **30** 191–6
[56] Phan-Thien N, Mai-Duy N and Khoo B C 2014 A spring model for suspended particles in dissipative particle dynamics *J. Rheol.* **58** 839–67
[57] Boromand A, Jamali S, Grove B and Maia J M 2018 A generalized frictional and hydrodynamic model of the dynamics and structure of dense colloidal suspensions *J. Rheol.* **62** 905–18
[58] Lees A W and Edwards S F 1972 The computer study of transport processes under extreme conditions *J. Phys. C: Solid State Phys.* **5** 1921
[59] Seto R, Mari R, Morris J F and Denn M M 2013 Discontinuous shear thickening of frictional hard-sphere suspensions *Phys. Rev. Lett.* **111** 218301
[60] Cox W P and Mer E H 1958 Correlation of dynamic and steady flow viscosities *J. Polym. Sci.* **28** 619–22
[61] Guazzelli É and Pouliquen O 2018 Rheology of dense granular suspensions *J. Fluid Mech.* **852** 1-73
[62] Krieger I M and Thomas J D 1959 A mechanism for non-Newtonian flow in suspensions of rigid spheres *Trans. Soc. Rheol.* **3** 137-152
[63] Sirk T W, Moore S and Brown E F 2013 Characteristics of thermal conductivity in classical water models *J. Chem. Phys.* **138** 064505
[64] Cheng X, McCoy J H, Israelachvili J N and Cohen I 2011 Imaging the microscopic structure of shear thinning and thickening colloidal suspensions *Science* **333** 1276–9
[65] Cheng X, Xu X L, Rice S A, Dinner A R and Cohen I 2012 Assembly of vorticity-aligned hard-sphere colloidal strings in a simple shear flow *Proc. Natl Acad. Sci. USA* **109** 63–7